

The limits of Near Field Immersion Microwave Microscopy evaluated by imaging bilayer graphene Moiré patterns

Douglas A. A. Ohlberg,¹ Diego Tami,² Andreij C. Gadelha,³ Eliel G. S. Neto,⁴
Fabiano C. Santana,³ Daniel Miranda,³ Wellington Avelino,² Kenji Watanabe,⁵
Takashi Taniguchi,⁵ Leonardo C. Campos,³ Jhonattan C. Ramirez,^{2,6} Cássio
Gonçalves do Rego,^{2,6} Ado Jorio,^{2,7,3} and Gilberto Medeiros-Ribeiro^{*2,8}

¹*Microscopy Center, Universidade Federal de Minas
Gerais, Belo Horizonte, MG 31270-901, Brazil*

²*Electrical Engineering Graduate Program, Universidade Federal
de Minas Gerais, Belo Horizonte, MG 31270-901, Brasil.*

³*Physics Department, Universidade Federal de Minas
Gerais, Belo Horizonte, MG 31270-901, Brazil.*

⁴*Instituto de Física, Universidade Federal da Bahia, Campus
Universitário de Ondina, Salvador - BA, 40170-115 Brazil.*

⁵*National Institute for Materials Science (NIMS),
1-2-1 Sengen, Tsukuba-city, Ibaraki 305-0047, Japan.*

⁶*Department of Electronic Engineering, School of Engineering, Universidade
Federal de Minas Gerais, Belo Horizonte, MG 31270-901, Brazil*

⁷*Technology Innovation Graduate Program, Universidade Federal
de Minas Gerais, Belo Horizonte, MG 31270-901, Brazil.*

⁸*Computer Science Department, Universidade Federal de
Minas Gerais, Belo Horizonte, MG 31270-901, Brazil*

Molecular and atomic imaging required the development of electron and scanning probe microscopies to surpass the physical limits dictated by diffraction [1]. Nano-infrared experiments [2] and pico-cavity tip-enhanced Raman spectroscopy imaging later demonstrated that radiation in the visible range [3] can surpass this limit by using scanning probe tips to access the near-field regime [4]. Here we show that ultimate resolution can be obtained by using scanning microwave imaging microscopy to reveal structures with feature sizes down to 1 nm using a radiation of 0.1 m in wavelength. As a test material we use twisted bilayer graphene, which is not only a very important recent topic due to the discovery of correlated electron effects such as superconductivity [5], but also because it provides a sample where we can systematically tune a superstructure Moiré pattern's modulation from below one up to tens of nanometers. By analyzing the tip-sample distance dynamics, we demonstrate that this ultimate 10^8 probe-to-pattern resolution can be achieved by using liquid immersion microscopy concepts and exquisite force control exerted on nanoscale water menisci.

Liquid immersion microscopy has its roots in observations made by Hooke in 1667 [6] that images would improve in clearness and brightness upon spreading fluids onto the surface and gently moving it upwards towards the lens until touching. Additionally, the adhesion of liquid to the lens was so robust and firm that it bore the investigated object being moved about the field of view. This vivid description of meniscus formation and usage was subsequently expanded in 1813 with Brewster’s concept of the oil immersion lens [7]. Later, in 1855, Amici improved upon several construction aspects, concerned primarily with diminishing the loss of light in high power microscopes by opting for water as the immersion liquid [7]. Ensuing developments that further addressed the issues of light loss and improvement of the magnification power of lenses consolidated the recognition of immersion lens microscopy as a well established technique.

Albeit remarkable, all these developments are diffraction limited, defined by the Abbé’s resolution limit of $d = \lambda/2n\sin\theta$, with $n\sin\theta$, as the numerical aperture. The proposal of scanning aperture imaging by Synge [4] for near field imaging was put into practice in 1972 by Ash [8], improving magnification beyond the Abbé limit with a figure of merit of λ/d of 60. Operation in the near field regime has since enabled a tremendous advance in microscopy, deserving a detailed and fair review that falls outside the scope of the present letter, as it would encompass implementations at many different wavelengths, construction details and application fields. In the microwave regimen there are interesting opportunities to be explored, as the field is at the crossroads of optics and electronics.

Scanning microwave impedance microscope (sMIM) is one of the latest additions to the family of scanning probe microscopes. Commercially available [9] tools can now be used to retrofit existing equipment, and exciting results in multiple applications have been published [10–12] describing exquisite spatial detail and vector analysis of the microwave reflected signal at each pixel. A 3 GHz microwave signal is coupled to an Atomic Force Microscope (AFM) probe tip that works as a waveguide and performs as an apertureless near-field microscope [10]. A key differentiating aspect of sMIM is that, unlike Scanning Tunneling Microscopy, its ability to image nano-scale modulations in the electronic and dielectric properties of complex structures is not restricted to conductive samples, but possible with insulating dielectrics as well. A point worth emphasizing, is that the capacitance signal conveys dielectric, geometric, and quantum information. Previously, Seabron [11] employed sMIM to assess quantum capacitance of carbon nanotubes. Capacitance spectroscopy is a

technique historically employed to map the electronic and quantum properties of quantum dots [13, 14] and two-dimensional quantum systems [15]. In these systems, a dielectric layer is mandatory for a proper adjustment of the chemical potential between probe electrode (gate, tip) and system of interest (quantum structure). Seabron [11] noted that to improve the spectroscopic resolution of sMIM, a high permittivity (high-k) capping layer would be essential to better couple the tip to the sample, and that adventitious water found on surfaces forming a meniscus could be an option. With $\varepsilon_r = \varepsilon/\varepsilon_0 \approx 80$ and a refractive index of 9 at 3 GHz frequencies, its surface ubiquity demands that the effect of water must be included in any modeling of sMIM experiments at ambient conditions.

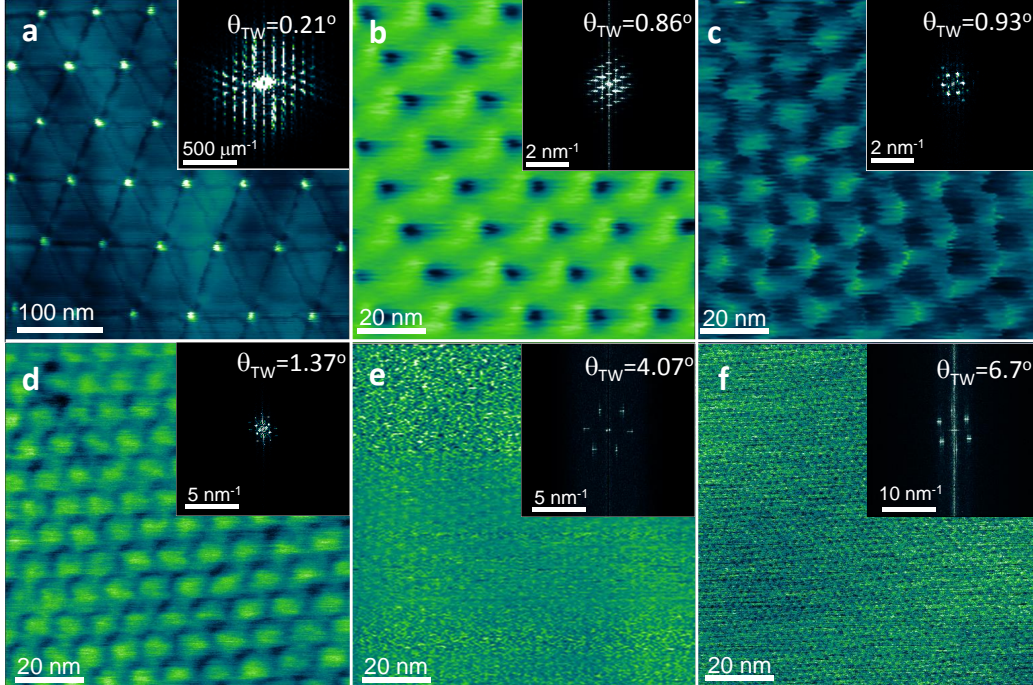


FIG. 1. **sMIM scans.** **a.** 400 nm x 400 nm conductance image of TBG:hBN:glass, with contrast arising from the juxtaposing of two graphene layers with $\theta_{TM} = 0.21^\circ$, and the strain soliton domain wall arising from surface reconstruction clearly resolved [16]. The false color is keyed to the intensity of reflected signal, white being the highest, i.e., higher conductance. The observed pattern is consistent with a reconstructed structure. The inset shows the corresponding FT. **b-f.** 100 nm x 100 nm scans exhibiting a wide range of angles and corresponding Moiré patterns. The systems examined are TBG:hBN:glass (**a**, **b**, **e**, **f**), TBG:SiO₂:Si **c**, and TBG:glass **d**.

Here we report sMIM results with unprecedented spatial resolution performed on Twisted Bilayer Graphene (TBG) systems of varying twist angles. TBG systems offer an exciting opportunity to create two-dimensional superlattices of varying periodicity in a conceptually simple strategy of adjusting the twist angle θ_{TM} between the two graphene layers. The search for systems producing two-dimensional periodic potential modulation in appropriate dimensions has seen a variety of implementations over the years, for example ranging from antidot lattices [17] and top-gate modulation [18] in 2D electron gases in III-V heterostructures in the 1990's, to more recent and exciting TBG embodiments [19]. The possibility to explore the potential modulation parameters in a more detailed fashion offered by the van der Waal heterostructures such as graphene presented surprising opportunities near the magical angle of $\approx 1.1^\circ$ that goes beyond metal-insulator transition and Wigner crystallization [18], allowing the observation of additional electron-correlation physics such as superconductivity [5]. Tools that can expeditiously analyze and provide answers on the electronic structure, preferably at ambient conditions, are currently being pursued [12, 16].

Figure 1 shows a series of sMIM scans over a set of twisted bilayer graphene (TBG) systems, with twist angles θ_{TM} of **a.** 0.21° , **b.** 0.86° , **c.** 0.93° , **d.** 1.37° , **e.** 4.07° and **f.** 6.7° . These samples were characterized by Raman spectroscopy, Tip Enhanced Raman Spectroscopy microscopy [20] and UHV-STM (see Materials and Methods Section for all the experimental details), to independently verify the bilayer locations and confirm the observed Moiré superlattices that arise in TBG systems. TBG systems are atomically flat, which conveniently eliminates surface topography contributions to the reflected microwave signal, leaving the underlying electronic and dielectric structure components in the admittance intact. Figure 1 demonstrates the ability of the sMIM to observe the solitonic structures that arise in the atomically reconstructed TBGs prepared with twist angles smaller than 1.1° [16] (figure 1 **a**) and many interesting features as we move through the relaxation transition (figures 1 **b.** through **f.**), thus establishing sMIM as an important tool to non-invasively examine these systems in ambient conditions. The false color scale is keyed to the intensity of the real part of the reflected microwave signal, i.e., the conductance component. Inspection of figure S3 shows how inextricably connected are the complex reflected microwave to the complex admittance of the sample. All the data shown here are non-filtered, and the only image processing performed was background removal and color range adjustment. In the upper right corner of each image, a Fourier Transform (FT) of the data is displayed, showing

diffraction spots corresponding to the periodic modulation of the electronic properties due to the Moiré two-dimensional superlattice. The sequence spans a wide range of periods, culminating in a 6.7° twist angle and a period $1/f$ of 2.1 nm for the sample in **f**.

The Nyquist frequency f_c , defined by the highest frequency that can be inferred from a signal requires a spatial resolution of at least $2f_c$ [21]. Thus, our resolution is better than 1.05 nm ($1/2f$), despite the fact that the tip radius is 50 times bigger. Considering the Abbé's limit, our figure of merit is 10^8 . This unprecedented resolution requires a deeper investigation.

The reflected microwave signal is a complex function that depends on substrate admittance (sample conductivity and permittivity, see figure S3 in supplemental material section), with the imaginary part related to the system capacitance. Examining the tip-surface approach curves tracing cantilever deflection and capacitance signal allows us to assess tip-surface mechanical and electrical coupling. The observed capacitance and force behavior during tip approach and retraction with respect to a TBG:hexagonal Boron Nitride (hBN):Glass stack are shown in black and red dotted lines in figures 2 **a**, **b**. The directions of approach and retraction on the capacitance data are indicated by arrows. At about ~ 10 nm sample-substrate distance, the tip experiences capillarity attraction (~ 7 nN force) and the capacitance jumps. At the onset of the tip deflection due to the attractive force of the meniscus, the x-axis no longer represent tip-surface distance but rather z-piezo displacement because of the cantilever elastic deformation towards the surface.

The data are fit to an analytical model for the capacitance between a tip and a surface [22], described by equation 1:

$$C_{\text{meas}} = C_{\text{stray}} + 2\pi\epsilon_0 R \ln[1 + R(1 - \sin \theta_0)/z] \quad (1)$$

with C_{stray} as the stray capacitance, ϵ_0 the vacuum permittivity, R as the tip radius, θ_0 the aperture angle, chosen to be about 10° [22], and z the tip height. The data and fit (thin green line with solid circles) are plotted as $\Delta C = C(z) - C(1 \mu\text{m})$, and multiplied by a normalizing constant. The tip radius R was kept fixed at 50 nm, its nominal value. The agreement between data and analytical model captures the capacitance dependence on z from $1 \mu\text{m}$ to about 50 nm from the surface.

To accurately describe the capacitance of a tip in close proximity to the surface, we performed Finite Element Method (FEM) [23] modeling using the COMSOLTM Multiphysics

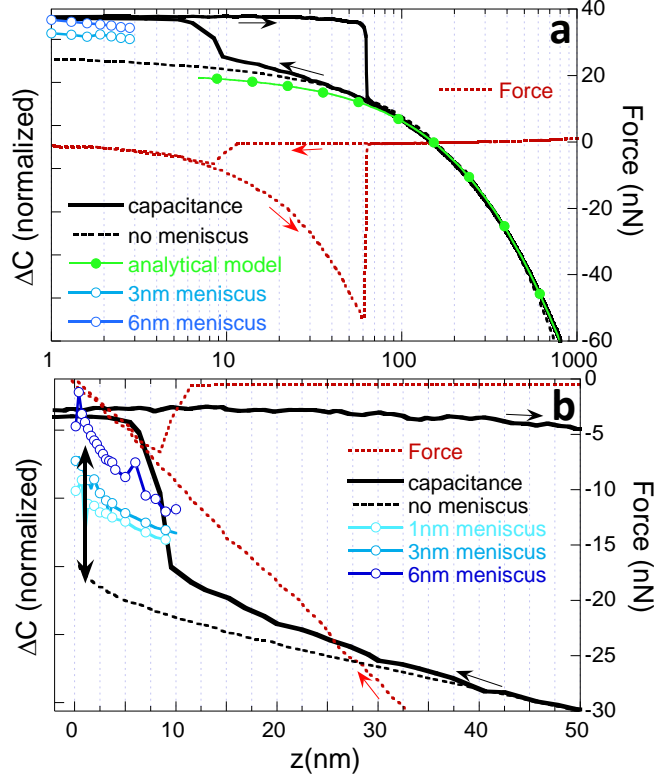


FIG. 2. **a.** The reference of $z = 0$ is defined on tip contact, which happens after the tip pull in by the meniscus, and subsequent motion z -piezo until the deflection reaches zero force. Negative z corresponds to pushing the tip into the repulsive mode. A typical force-curve approach of a WTi metallic tip towards the TBG layer. In red the cantilever deflection and corresponding force. The black solid line corresponds to the measured capacitance signal. The green line with solid circles correspond to a fit of the data to equation 1, with the tip radius fixed at 50nm. The black, dashed line represents the FEM model assuming a 1nm water layer on both surfaces. The blue empty circles correspond to the FEM model of the system assuming a water meniscus of 3nm and 6nm radii, respectively, with the thickness as the independent variable z . **b.** Close up of the same data, in a linear plot in the vicinity of meniscus formation and snap off. The arrows indicate the tip direction, with the corresponding colors for capacitance (black) and force (red).

simulation tool taking into account the contribution of both adventitious water and meniscus formation to the measured capacitance (see details in suppl. materials, figure S2). Water is ubiquitous and frequently considered an unwanted nuisance that complicates nano-scale phenomena, although it has been used as a resource (see, for example [24]). Its role in the theory of capillary forces has also been exhaustively studied ever since Hooke's work with

water menisci, and his observations can today be precisely assessed with any commercially available or home made microscopes to the degree that understanding of capillarity has advanced to the nanoscale. AFM embodies one of the most convenient tools to probe capillarity at the nanoscale level. Experiments covering meniscus dynamics formation [25] and meniscus stiffness [26] illustrate the level of control and understanding that has been achieved of the tip-water meniscus-surface system. This body of knowledge can be used to engineer menisci at the nanoscale, since precise control of force and tip velocity [25], and environmental conditions can be done routinely nowadays.

The capacitance dependence on z derived from the FEM model is shown as a black dashed line for a system with adventitious water of 1 nm on the tip and surface, and empty circles in different shades of blue for the additional contribution of water meniscus of 2-6 nm radii [25] and varying thickness. The model captures the capacitance dependence on z for most of the experimental range, except at the onset of meniscus formation. This excess capacitance can be accounted for by the meniscus nucleation process. In the literature, the proposed values for meniscus thickness are of the order of 0.2 nm in close proximity [27] to 1.65 nm at snap-off [28]. Calculated values of meniscus of constant radii and decreasing thickness (z axis) at the 0.2-1.65 nm in blue circles in figure 2b show a reasonable agreement with the measured capacitance jump (indicated by the double arrow). Within the simplifying assumptions for the proposed geometry, amount of water on the surfaces, dynamics of menisci formation, and capacitive forces [22] that may pull the tip closer, the capacitance behavior derived from the simulated model captures the essence of the tip approach and meniscus formation and closely matches the experimental data and analytical model. A more detailed evolution of tip retraction and capacitance decrease of the tractioned meniscus [26] is shown in supplemental figures S4 a,c.

The dynamic aspect of meniscus formation [25], which for tip approach is of the order of a few ms, impacts not only the force-curve approach curves but scanning generally speaking. In fact, for the scan rates employed (1 $\mu\text{m/s}$ for figure 1.c) the estimated meniscus radius is 2 nm [25]. As an additional test to corroborate the presence of a meniscus, we performed experiments in the so called NAP mode (see supplemental material), which basically is a set of two consecutive line scans, one in non-contact and the second at a pre-defined lift height. We were able to continue imaging at lift heights of up to 50 nm piezo displacement (see figure S4 in the supplemental material section), with a minor capacitance drop ($\sim 0.01\Delta C$)

and sustained meniscus presence. We never observed any image contrast in AC driven intermittent contact (or tapping) mode imaging in our experiments, which could be due to a poor or nonexistent meniscus formation (tip oscillation frequency of 70 kHz, and therefore a period of $1.4 \mu\text{s}$ which could be too short [25]). Operation in repulsive mode led to tip wear and sample damage, and not necessarily better imaging conditions.

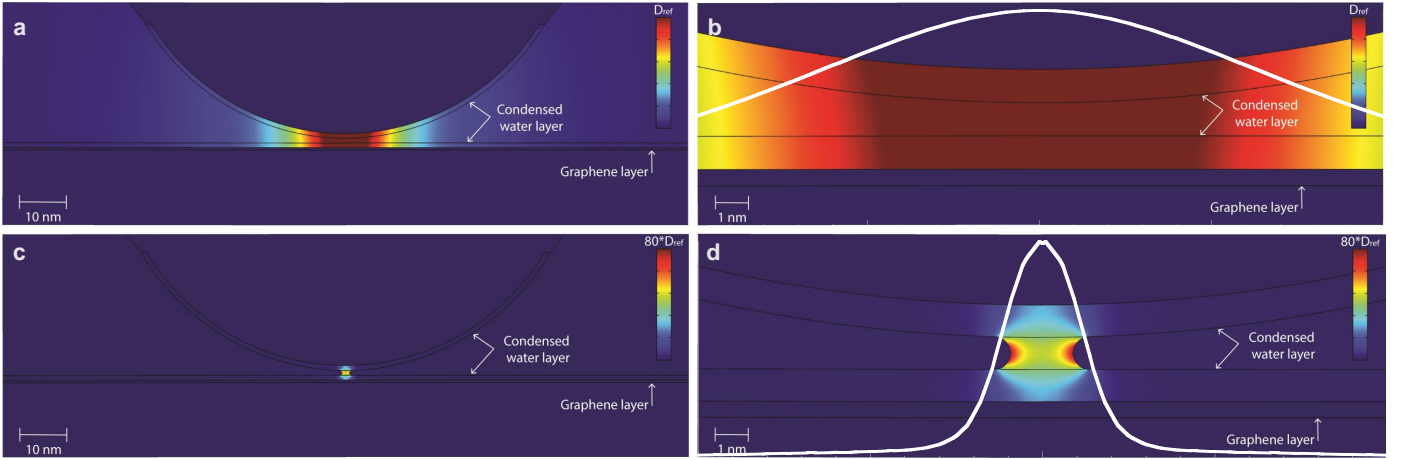


FIG. 3. **Electric displacement field distribution in the tip/sample simulated structure.**

$\mathbf{D}_{Ref} = 2.5 \times 10^{-3} \text{C/m}^2$ **a.** Tip/sample simulated system for Graphene:hBN:Glass substrate at 1 nm z distance without meniscus, and a 1nm layer of water on both surfaces. **b.** Close-up on the structure detailed in **a**. **c.** Simulation for the same structure in **a**, with the additional implementation of a water meniscus. The color range has been expanded by $\mathbf{D}_{fullscale} = 80 \mathbf{D}_{Ref}$ in order to permit the visualization of the increased density in \mathbf{D} . **d.** Close-up the structure detailed in **c**, also with the expanded scale. Line profiles of the normalized Electric Displacement Field $\mathbf{D}_{fullscale} = 1$ are superposed onto the image and demonstrates the concentration effect of the water meniscus.

In Figure 3 we examine the field distribution in the vicinity of and inside the water meniscus at the onset of meniscus formation (assumed to happen at 1 nm). The FEM

calculated distribution of $\mathbf{D} \equiv \varepsilon_0 \mathbf{E} + \mathbf{P}$ over the entire system and its evolution during tip approach can be seen in the videos **SV1** in supplemental material. The simulation results shown in figure 3 exhibit the configurations of tip-substrate without meniscus figures 3 **a,b** and with meniscus figures 3 **c,d**, on top of a TBG layer. The majority of the displacement field is localized at the apex of the tip upon meniscus formation, but noteworthy is the fact that it concentrates at the water:TBG interface, as seen in the \mathbf{D} profiles (white lines) in figures 3 **b,d**. The effect of the meniscus demonstrates the ability to concentrate fields in very small regions, corroborating the modeled and experimentally observed capacitance jumps. From a microwave perspective, the meniscus is an iris that upon force control and operation in the attractive mode allows for impedance matching and field concentration. Thus, menisci can be used to augment near-field resolving power.

Finally, rigorous methods for evaluation of resolution rely on well defined Point Spread Functions (PSF) from which one can deduce the Transfer Function of the optical system. That would allow us to verify the resolution beyond the Nyquist limit that represents an upper bound. The challenge of identifying a point-like defect to extract the ultimate resolution along with additional correlation analysis is discussed in the supplemental material section.

Near field and immersion optics at microwave frequencies create opportunities worth exploring. One convenient aspect of sMIM is the lack of externally coupled optical apparatus, enabling connectorized tools for easy deployment. Further possibilities can be envisioned for near field immersion microscopy. The water layer requirement may for instance allow examination of biological samples, using single layer talc or hBN sheets as cover-slips for adequate microwave transmission. The ability to implement spatially resolved capacitance spectroscopy by means of DC biasing schemes is an exciting prospect, becoming an invaluable tool for van der Waals heterostructures and band-gap engineering. An often explored resource of scanning probe microscopy is nanolithography. Yet, for the majority of the tools employed in nanolithography, the embodiments are normally implemented in an open loop fashion, allowing only post-mortem inspection. With the reflected microwave signal, one can close the loop and monitor the complex impedance of the region of interest, while performing the patterning [29]. An immediate implementation in the already vast field of dip-pen nanolithography [30] would envision tracking both the real and imaginary parts of the reflected microwave signal to enable real time tracking of minute quantities of dispensed

materials, each with its impedance signature.

References

- [1] E. Abbe. VII.-on the estimation of aperture in the microscope. *Journal of the Royal Microscopical Society*, 1(3):388–423, June 1881.
- [2] Jianing Chen, Michela Badioli, Pablo Alonso-González, Sukosin Thongrattanasiri, Florian Huth, Johann Osmond, Marko Spasenović, Alba Centeno, Amaia Pesquera, Philippe Godignon, Amaia Zurutuza Elorza, Nicolas Camara, F. Javier García de Abajo, Rainer Hillenbrand, and Frank H. L. Koppens. Optical nano-imaging of gate-tunable graphene plasmons. *Nature*, 487(7405):77–81, June 2012.
- [3] Joonhee Lee, Kevin T. Crampton, Nicholas Tallarida, and V. Ara Apkarian. Visualizing vibrational normal modes of a single molecule with atomically confined light. *Nature*, 568(7750):78–82, April 2019.
- [4] E.H. Synge. XXXVIII.a suggested method for extending microscopic resolution into the ultra-microscopic region. *The London, Edinburgh, and Dublin Philosophical Magazine and Journal of Science*, 6(35):356–362, August 1928.
- [5] U. Zondiner, A. Rozen, D. Rodan-Legrain, Y. Cao, R. Queiroz, T. Taniguchi, K. Watanabe, Y. Oreg, F. von Oppen, Ady Stern, E. Berg, P. Jarillo-Herrero, and S. Ilani. Cascade of phase transitions and dirac revivals in magic-angle graphene. *Nature*, 582(7811):203–208, June 2020.
- [6] Robert Hooke. *Lecture and Collections, Microscopium*. J. Martyn, Printer to the Royal Society, London, 1667. Discourse and Description of Microscopes, improved for discerning the nature and texture of Bodies.
- [7] S. Bradbury. *The Evolution of the Microscope*. Pergamon, 1967.
- [8] E. A. Ash and G. Nicholls. Super-resolution aperture scanning microscope. *Nature*, 237(5357):510–512, June 1972.
- [9] *ScanWave Pro*, (accessed June 22, 2020). <http://www.primenanoinc.com>.
- [10] Oskar Amster, Fred Stanke, Stuart Friedman, Yongliang Yang, St.J. Dixon-Warren, and B. Drevniok. Practical quantitative scanning microwave impedance microscopy. *Microelec-*

- tronics Reliability*, 76-77:214–217, September 2017.
- [11] Eric Seabron, Scott MacLaren, Keith Jones, and William L. Wilson. A dynamic-difference approach to scan probe microwave reflectivity mapping of the nanoscale electronic properties of single-walled carbon nanotubes. *Journal of Applied Physics*, 125(17):174303, May 2019.
 - [12] Kyunghoon Lee, M. Iqbal Bakti Utama, Salman Kahn, Appalakondaiah Samudrala, Nicolas Leconte, Birui Yang, Shuopei Wang, Kenji Watanabe, Takashi Taniguchi, Guangyu Zhang, Alexander Weber-Bargioni, Michael Crommie, Paul D. Ashby, Jeil Jung, Feng Wang, and Alex Zettl. Ultra-high-resolution imaging of moiré lattices and superstructures using scanning microwave impedance microscopy under ambient conditions, arxiv:2006.04000, 2020.
 - [13] R. C. Ashoori, H. L. Stormer, J. S. Weiner, L. N. Pfeiffer, S. J. Pearton, K. W. Baldwin, and K. W. West. Single-electron capacitance spectroscopy of discrete quantum levels. *Physical Review Letters*, 68(20):3088–3091, May 1992.
 - [14] T. P. Mayer Alegre, F. G. G. Hernández, A. L. C. Pereira, and G. Medeiros-Ribeiro. Landé g-Tensor in semiconductor nanostructures. *Physical Review Letters*, 97(23), December 2006.
 - [15] G. L. Yu, R. Jalil, Branson Belle, Alexander S. Mayorov, Peter Blake, Frederick Schedin, Sergey V. Morozov, Leonid A. Ponomarenko, F. Chiappini, S. Wiedmann, Uli Zeitler, Mikhail I. Katsnelson, A. K. Geim, Kostya S. Novoselov, and Daniel C. Elias. Interaction phenomena in graphene seen through quantum capacitance. *Proceedings of the National Academy of Sciences*, 110(9):3282–3286, February 2013.
 - [16] Leo J. McGilly, Alexander Kerelsky, Nathan R. Finney, Konstantin Shapovalov, En-Min Shih, Augusto Ghiotto, Yihang Zeng, Samuel L. Moore, Wenjing Wu, Yusong Bai, Kenji Watanabe, Takashi Taniguchi, Massimiliano Stengel, Lin Zhou, James Hone, Xiaoyang Zhu, Dmitri N. Basov, Cory Dean, Cyrus E. Dreyer, and Abhay N. Pasupathy. Visualization of moiré superlattices. *Nature Nanotechnology*, June 2020.
 - [17] K. Ensslin and P. M. Petroff. Magnetotransport through an antidot lattice in GaAs-AlxGa1-xAs heterostructures. *Physical Review B*, 41(17):12307–12310, June 1990.
 - [18] T Schlösser, K Ensslin, J. P Kotthaus, and M Holland. Internal structure of a landau band induced by a lateral superlattice: a glimpse of hofstadter's butterfly. *Europhysics Letters (EPL)*, 33(9):683–688, March 1996.
 - [19] C. R. Dean, L. Wang, P. Maher, C. Forsythe, F. Ghahari, Y. Gao, J. Katoch, M. Ishigami, P. Moon, M. Koshino, T. Taniguchi, K. Watanabe, K. L. Shepard, J. Hone, and P. Kim.

- Hofstadter's butterfly and the fractal quantum hall effect in moiré superlattices. *Nature*, 497(7451):598–602, May 2013.
- [20] Andreij C. Gadelha, Douglas A. A. Ohlberg, Cassiano Rabelo, Eliel G. S. Neto, Thiago L. Vasconcelos, João L. Campos, Jessica S. Lemos, Vinícius Ornelas, Daniel Miranda, Rafael Nadas, Fabiano C. Santana, Kenji Watanabe, Takashi Taniguchi, Benoit van Troeye, Michael Lamparski, Vincent Meunier, Viet-Hung Nguyen, Dawid Paszko, Jean-Christophe Charlier, Leonardo C. Campos, Luiz G. Cançado, Gilberto Medeiros-Ribeiro, and Ado Jorio. Lattice dynamics localization in low-angle twisted bilayer graphene. arXiv:2006.09482, 2020.
- [21] J. Proakis and D. Manolakis. *Digital Signal Processing: Principles, Algorithms, and Applications*. Macmillan Publishing Company, 1992.
- [22] S. Hudlet, M. Saint Jean, C. Guthmann, and J. Berger. Evaluation of the capacitive force between an atomic force microscopy tip and a metallic surface. *The European Physical Journal B*, 2(1):5–10, April 1998.
- [23] Volakis, J. L., Chatterjee, A., Kempel, L. C. *Finite Element Method Electromagnetics: Antennas, Microwave Circuits, and Scattering Applications*. Wiley Interscience, 1998.
- [24] Guanglei Cheng, Pablo F. Siles, Feng Bi, Cheng Cen, Daniela F. Bogorin, Chung Wung Bark, Chad M. Folkman, Jae-Wan Park, Chang-Beom Eom, Gilberto Medeiros-Ribeiro, and Jeremy Levy. Sketched oxide single-electron transistor. *Nature Nanotechnology*, 6(6):343–347, April 2011.
- [25] Robert Szoszkiewicz and Elisa Riedo. Nucleation time of nanoscale water bridges. *Physical Review Letters*, 95(13), September 2005.
- [26] Simon Carpentier, Mario S. Rodrigues, Miguel V. Vitorino, Luca Costa, Elisabeth Charlaix, and Joël Chevrier. Out of equilibrium anomalous elastic response of a water nano-meniscus. *Applied Physics Letters*, 107(20):204101, November 2015.
- [27] Miroslav Bartošík, Lukáš Kormoš, Lukáš Flajšman, Radek Kalousek, Jindřich Mach, Zuzana Lišková, David Nezval, Vojtěch Švarc, Tomáš Šamořil, and Tomáš Šikola. Nanometer-sized water bridge and pull-off force in AFM at different relative humidities: Reproducibility measurement and model based on surface tension change. *The Journal of Physical Chemistry B*, 121(3):610–619, January 2017.
- [28] O H Pakarinen, A S Foster, M Paaanen, T Kalinainen, J Katainen, I Makkonen, J Lahtinen, and R M Nieminen. Towards an accurate description of the capillary force in

- nanoparticle-surface interactions. *Modelling and Simulation in Materials Science and Engineering*, 13(7):1175–1186, September 2005.
- [29] David A. Champion, James Abbot, Raymond Adamic, Gilberto Ribeiro, Cassio Goncalves, Diego Tami, Wellington Avelino, and Douglas Pederson. Near-field monitoring of energy delivery. (Wipo Patent application WO/2019/152035), 2019.
- [30] Guoqiang Liu, Sarah Hurst Petrosko, Zijian Zheng, and Chad A. Mirkin. Evolution of dip-pen nanolithography (DPN): From molecular patterning to materials discovery. *Chemical Reviews*, April 2020.

Materials and Methods

Scanning microwave impedance microscopy: The AFM used to support the SMIM acquisition was a MFP-3D-SA manufactured by Asylum Research. The shielded co-axial AFM probes as well as the electronics unit (model Scanwave Pro) used to transmit and measure the microwave signal were manufactured by PrimeNano Inc. The experiment schematics are shown in figure S1 of the supplemental material section. All SMIM and AFM data were collected under ambient conditions. Scanning tunneling microscopy (STM): STM data were collected with a UHV VT STM/AFM model manufactured by Omicron GmbH. The tips used were etched tungsten probes. The STM was calibrated with a standard graphite lattice observed on an HOPG surface and a Si (111) reconstructed 7 X 7 surface lattice. All STM data were collected at room temperature at a pressure of 1×10^{-10} Torr. The Moiré patterns observed by STM were obtained from TBG samples initially supported by oxide-coated Si coupons for sMIM inspection. The bilayers were then, transferred to conducting, gold-coated mica coupons for subsequent STM analysis.

Tip-enhanced Raman spectroscopy (TERS): The nano-Raman system used for the TERS analysis was a hybrid configuration combining micro-Raman optics with an atomic force microscope that was assembled in-house. The system employs an inverted optical microscope that by means of an oil immersion objective (1.4 numerical aperture) tightly focuses a radially polarized HeNe excitation laser source (633 nm) onto the AFM/TERS probe and local surface being scanned by the probe. The AFM/TERS probes are especially designed to resonate with the excitation laser producing highly localized field enhancements which are then back-scattered by the analyte sample into the spectrometer and charge-couple

device (CCD) that collects the Raman signal [20]. All TERS experiments in this work were conducted under ambient conditions.

Preparation of TBG: The twisted bilayer samples analyzed were prepared using a novel technique we have developed that is a variation of conventional, dry transfer, tear-and-stack methods [20]. Unlike other procedures, which either completely encapsulate graphene bilayers within a top and bottom layer of h-BN flakes or a bottom layer of h-BN flake and a top layer of polymer that often requires removal in subsequent solvent soaks and sample bakes, our dry transfer procedure fabricates simple, extremely clean, and unencapsulated TBGs free of polymers that can introduce undesired contaminants. The procedure relies on a special stamp design consisting of a truncated, polymer pyramid fabricated on a handle substrate that is not only capable of performing tear-and-stack operations on the initial graphene, but also allows subsequent detachment of the bilayer onto a variety of support substrates. (See supplemental) The substrate supports included simple glass coverslips with and without h-BN coating layers that were used for tip-enhanced Raman spectroscopy (TERS) analysis, mica coupons coated with atomically-flat gold for STM analysis, and silicon coupons coated with an 275nm oxide. After transfer to a respective substrate, a WITec Alpha 300 SAR confocal Raman Microscope was used for Raman spectroscopy and spatial mapping. These measurements were typically performed using a 633 nm laser, power of 5 mW, and spot size of 600 nm.

Acknowledgments

The authors acknowledge financial support from CNPq, FINEP, FAPEMIG, INCT Nanomateriais de Carbono, and CAPES.

Competing financial interests

The authors declare no competing financial interests

Author contributions

Sample preparation: Andreij C. Gadelha, Daniel Miranda, Fabiano C. Santana, Eliel G. S. Neto, Leonardo C. Campos; K. Watababe and T. Taniguchi provide hBN crystals; **Micro-Raman and TERS measurements:** Andreij C. Gadelha, Eliel G. S. Neto; **SPM measurements:** Douglas A. A. Ohlberg, Gilberto Medeiros-Ribeiro; **Finite Element Computation:** Diego Tami, Jhonattan C. Ramirez, Cássio Gonçalves do Rego; **Microwave technical support:** Wellington Avelino, Gilberto Medeiros-Ribeiro; **Data Analysis:** Gilberto Medeiros-Ribeiro, Douglas A. A. Ohlberg; **Project idealization and guidance:** Ado Jorio, Jhonattan C. Ramirez, Cássio Gonçalves do Rego and Gilberto M. Ribeiro; **Paper writing:** Douglas A. A. Ohlberg and Gilberto Medeiros-Ribeiro. Some authors contributed with parts of the text and figures, and they all read and agreed on the final version of the manuscript.

Supplemental Materials

EXPERIMENTAL SETUP

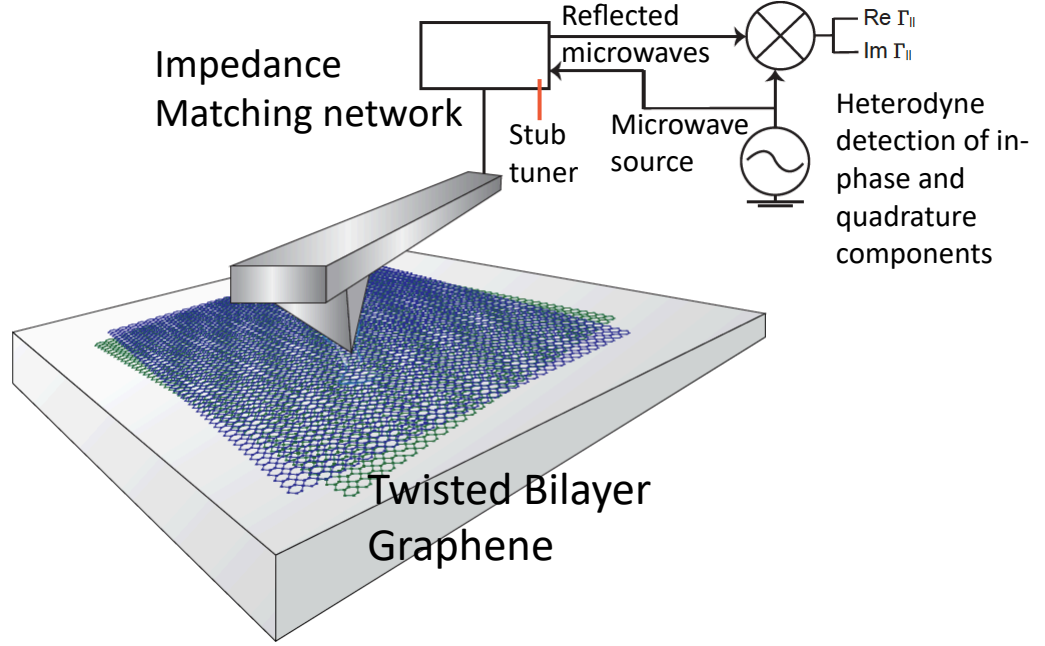


FIG. S1. Experimental set up showing the microwave circuitry for sample probing.

FINITE ELEMENT METHOD CALCULATIONS

Aiming to fully understand the effects observed in the measurements obtained by our scanning Microwave Impedance Microscopy (sMIM) system, some numerical simulations were performed implementing the Finite Element Method (FEM) [S1] in the COMSOLTM Multiphysics simulation tool, in order to calculate the tip-sample admittance.

The sMIM system was simulated in an axisymmetrical two-dimensional environment, i.e., taking the axial symmetry boundaries (at $r = 0$) into account, and consequently add an axial symmetry node to the component, which becomes valid just on the axial symmetry boundaries, figure 1, in order to reduce the computational cost of the simulation performed [S2]. The implemented tip has an inverted pyramid shape, with $8 \mu\text{m}$ at the top and $10 \mu\text{m}$ in

height. The structural characteristics of the implemented simulation system, can be seen in figure. S2.

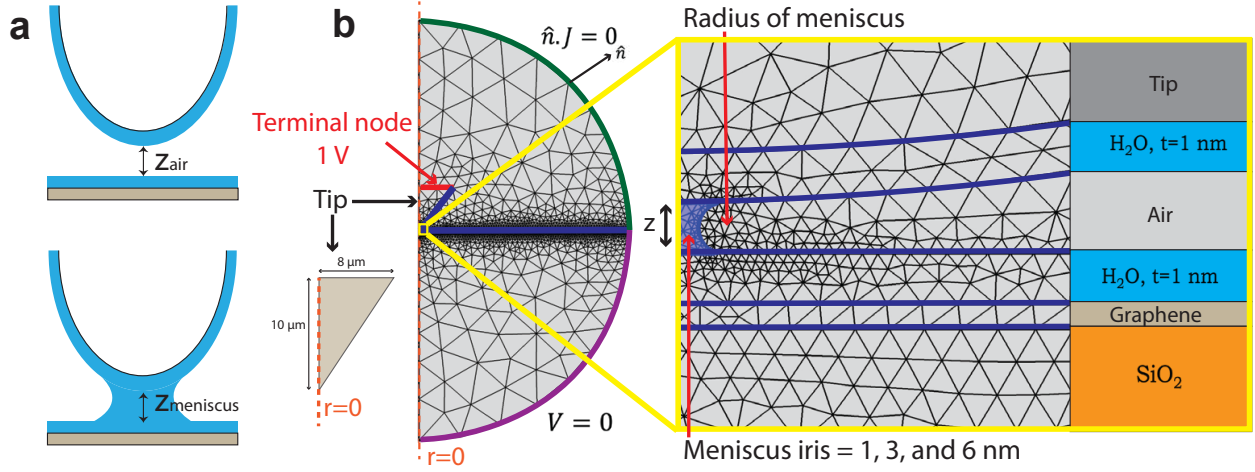


FIG. S2. Simulation structure. **a.** Tip and surface/sample with and without meniscus. **b.** Scheme of highlighting boundary conditions at electrical isolation and ground potential (zero potential). Radius of the tip, 50 nm. Simulated twisted double layer graphene on SiO₂:Si, assuming a 0.5 nm thick TBG with $\sigma = 10^6$ S/m and a 275nm thick SiO₂ with $\epsilon_r = 4$.

As presented in figure S2, the gap between the tip and the sample is just a few nanometers, providing the ideal conditions for the formation of a nanometric-order bridge between the tip of the simulated sMIM and the surface, due to the capillary condensation of water in our system, as described in the main text.

In a real measurement system, the admittance varies as function of the distance z . As the tip approaches the surface, the condensed water particles form the meniscus, depending on tip-surface. The simulations carried out contemplate two different scenarios, with and without the presence of the water meniscus, using a mesh with 13,000 total elements, of which 1,500 correspond to the elements in the contour conditions.

For systems with high frequency, the imaginary component of the admittance, the susceptance contribution, becomes many orders of magnitude larger than the real component, the conductive contribution.

$$C = \frac{\text{Im}(Y)}{\omega}, \quad (\text{S1})$$

where Y is the admittance, C is the capacitance, and $\omega = 2\pi f$ is the angular frequency

at $f = 3$ GHz.

Finally, the real and the imaginary part of the admittance were calculated as a function of the permittivity and the conductivity of the sample, the results corresponding to 1 nm meniscus on two single layer graphene over SiO_2 can be seen in figure S3.

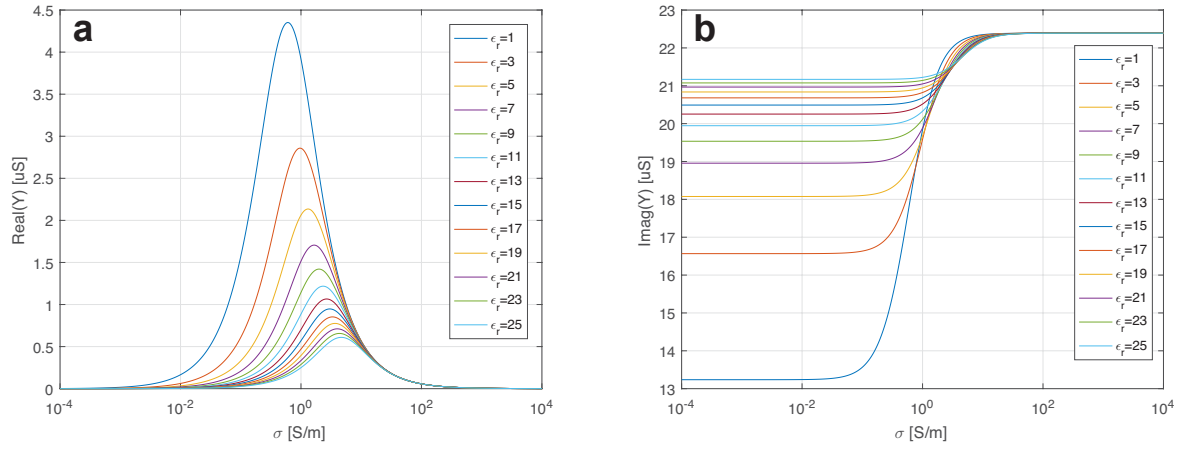


FIG. S3. **a** Real and **b** Imaginary part of the admittance as a function of the conductivity and permittivity

INDEPENDENT CONFIRMATION BY SCANNING TUNNELING MICROSCOPY

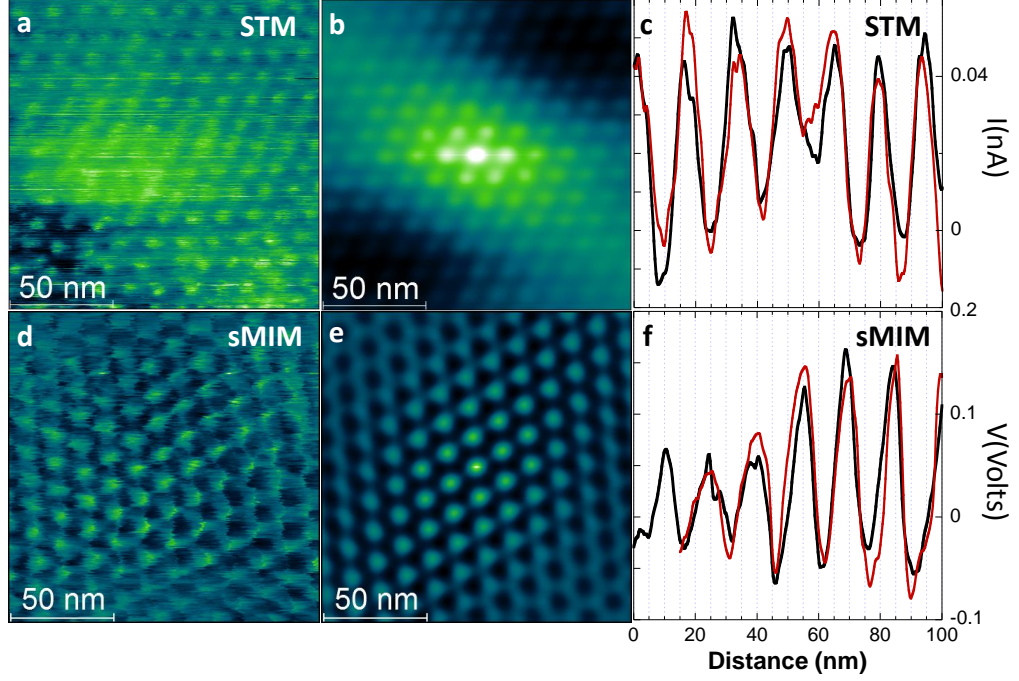


FIG. S4. **Comparison between STM and sMIM data.** **a.** 150 nm x 150 nm STM current image, **b.** its corresponding autocorrelation function and **c.** line profiles along the symmetry axis, **d.** 150 nm x 150 nm sMIM conductance image, **e.** its corresponding autocorrelation function, and **f.** line profiles along the symmetry axis.

In order to confirm the observation of the Moiré superlattices by sMIM, we perform Ultra-High Vacuum Scanning Tunneling Microscopy (UHV-STM). The samples were transferred from the glass substrate to a Au:Mica substrate and brought into the UHV system. The precise flake location was determined by a macro lens system that allowed a 10 μm resolution. We were able to get images from regions of similar twist angles ($\theta_{TM}=0.93^\circ$ for the sMIM experiments and $\theta_{TM}=1.10^\circ$ for the STM experiments). Figure S4 shows the image data, autocorrelation functions and line profiles for the STM (top row) and sMIM (bottom row).

DISCUSSION ON PSF

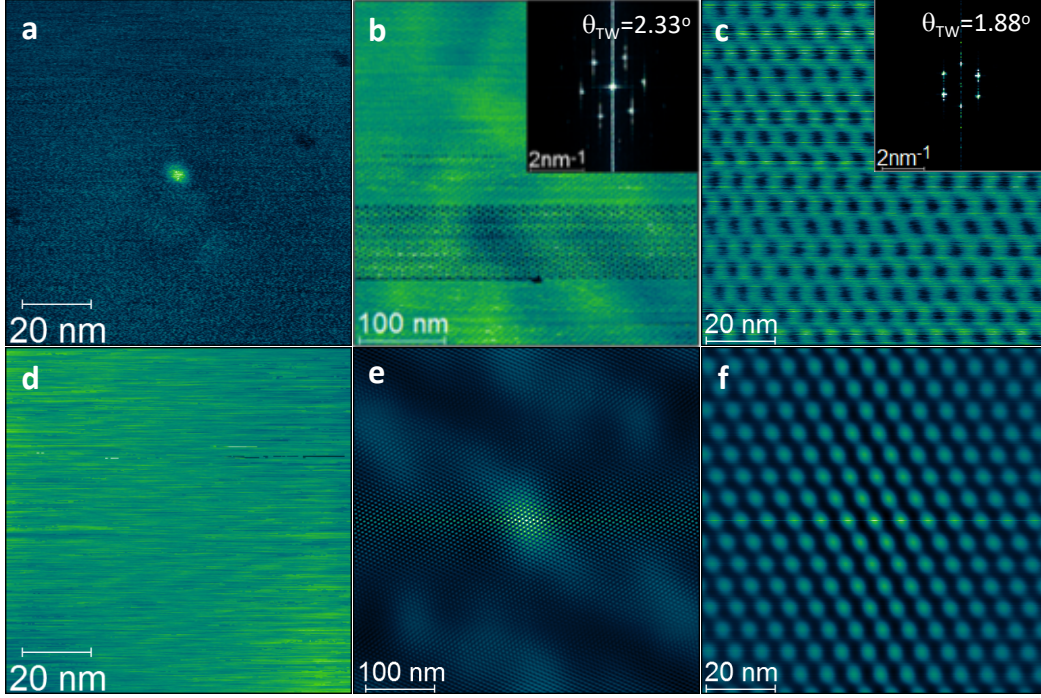


FIG. S5. **a**. 100 nm x 100 nm sMIM scan with an isolated defect on a otherwise flat piece of graphene. **b**. 400 nm sMIM scan on a TBG with $\theta_{TM} = 2.33^\circ$. **c**. 100 nm sMIM scan on a TBG with $\theta_{TM} = 1.88^\circ$. **d**. 100 nm x 100 nm topographic image corresponding to **a**, with a 300 pm full scale color scale. **e** Autocorrelation Function (ACF) taken on image **b**, showing a long range order, and **f** ACF taken on image **c**, showing a high degree of order.

Figure S5**a** shows a 100 nm x 100 nm sMIM scan with an isolated defect on a otherwise flat piece of graphene (figure S5**d** as the topography channel, 300 pm color scale range). This isolated object has a full width-half maximum of about 8 nm, but still bigger than an ideal PSF, since we were able to infer a resolution better than 1.05 nm. Yet, this isolated structure permits us to rule out tip artifacts that would otherwise create higher periodicity. Figure S5**b** shows a 400 nm sMIM scan on a TBG with $\theta_{TM} = 2.33^\circ$ and Figure S5**e** its corresponding autocorrelation function (ACF). Inspection of the autocorrelation function reveals minute details such as long range order and the existence of texture, shear stress and other defects, information that is essential for modeling the electronic properties of these

systems. Finally, figureS5**c** and **f** show a 100 nm sMIM scan on a TBG with $\theta_{TM} = 1.88^\circ$ and its corresponding ACF. Moiré patterns had been used before in the geometrical optics context by deflectometry for the determination of the Modulation transfer Function of optical systems[S3]. For this particular system, despite the fact that the FT unequivocally shows the periodicity of $1/2.1 \text{ nm}^{-1}$, autocorrelation functions shown in figures S5**e** and **f** that contain essentially the same information as the FT permit nevertheless a better assessment of the imaged surface, and also how uniform and long range order present in the surface, ruling out tip artifacts.

NAP EXPERIMENTS

The NAP experiments have a key goal to further substantiate the presence and use of the water meniscus as an imaging device. The term “nap pass” is used by Asylum Research that refers to an expression used in aviation “nap-of-the-earth flight,” that describes flight made at low altitude which closely tracks the contours of the underlying terrain [S6]. The experiment is performed in two steps: 1) one pass in contact or non-contact mode in order to extract the topography; and 2) a second pass at a predetermined height Δz above the surface using the topography information acquired in the previous scan in order to maintain the tip-substrate distance constant. This protocol is executed in a line-by-line fashion, in order to avoid sample drift. The convenience of a flat sample is instrumental to allow a unequivocal assessment of the capacitance and conductance signal. For this particular sample, the majority of the contrast was measured in the conductance channel, indicating a sample conductivity above 10 S/m, as seen in figure S3. Yet, the capacitance contains the meniscus information, and comparing its value in contact and lift mode permits us to assess some degree of meniscus deformation, rule out the possibility of a metallic fragment as the sole component responsible for the resolution, and evaluate any potential contrast change associated with meniscus deformation due to the cantilever lift.

Figures S6 **a** and **c** are expanded portions of figure 2**a** and **b**, to help visualize the capacitance decrease (black solid lines) and concurrent force (red solid lines) measurements during the lift mode. The filled circles in figure S6**c** represent the capacitance drops at different lift heights, evaluated from the sMIM capacitance images. The first observation is that although for small lifts the tip-retraction curve (solid back line) is still in agreement with the capacitance change observed in lift mode, it does not decrease as notably. The interpretation for this difference is related primarily with meniscus formation dynamics [S4, S5]. During the lift scan, the tip stays at a constant height thus providing more time for meniscus nucleation. The expected impact on the capacitance difference is consequently a smaller decrease because of a higher volume meniscus, as observed. Examining the conductance channel images displayed in figures S6**b**, contact, and S6**d**, we observe that imaging is still adequately performed for a lift of 50 nm (also see the green circle in figure S6**c**). The inset shows the auto-correlation functions, showing minimal changes in correlation lengths and same periodicity. The color scale nevertheless shows a decrease in signal amplitude for

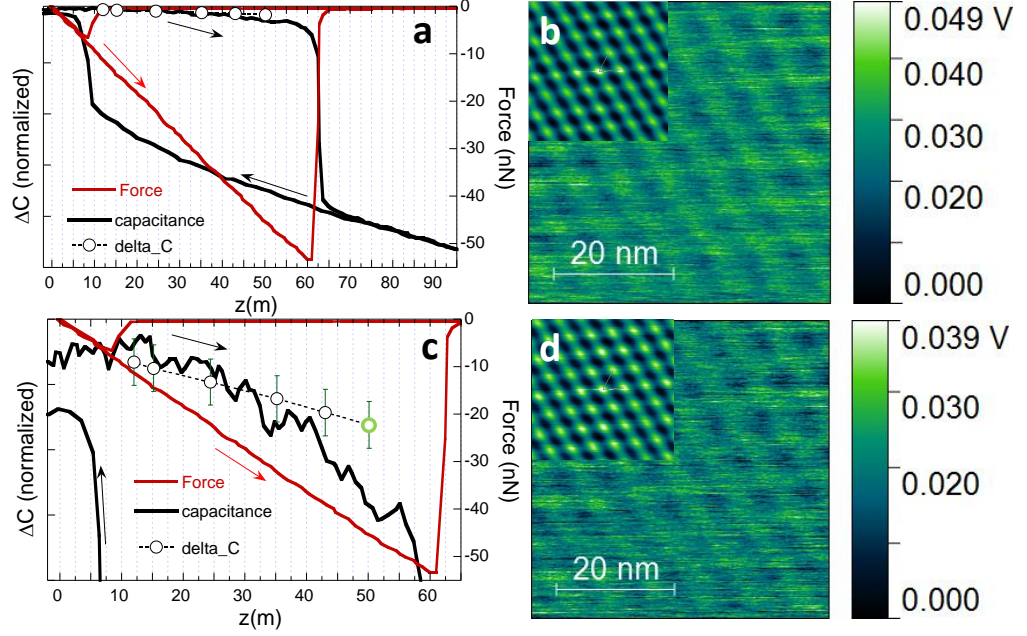


FIG. S6. NAP experiments: close up on figure 2: **a** and **c** Force-curve (red line) and capacitance (black line) approach of a tip towards a TBG:hBN:Glass system. The empty circles correspond to capacitance changes evaluated from the difference in capacitance images taken in lift mode from the contact mode as a function of Δ_z ; the error bars correspond to the RMS values at each image; **b** conductance image in contact mode, **d** conductance image with a tip lift of 50 nm. The insets show the autocorrelation functions for both images.

the image acquired in the lift mode, consistent with a more decoupled system because of a stretched meniscus.

References

-
- [S1] Volakis, J. L., Chatterjee, A., Kempel, L. C. *Finite Element Method Electromagnetics: Antennas, Microwave Circuits, and Scattering Applications*. Wiley Interscience, 1998.
 - [S2] M. Koshiba and K. Inoue. Simple and efficient finite-element analysis of microwave and optical waveguides. *IEEE Transactions on Microwave Theory and Techniques*, 40(2):371–377, 1992.

- [S3] I. Glatt, A. Livnat, and O. Kafri. Direct determination of modulation transfer function by moiré deflectometry. *Journal of the Optical Society of America A*, 2(2):107, February 1985.
- [S4] Robert Szoszkiewicz and Elisa Riedo. Nucleation time of nanoscale water bridges. *Physical Review Letters*, 95(13), September 2005.
- [S5] Simon Carpentier, Mario S. Rodrigues, Miguel V. Vitorino, Luca Costa, Elisabeth Charlaix, and Joël Chevrier. Out of equilibrium anomalous elastic response of a water nano-meniscus. *Applied Physics Letters*, 107(20):204101, November 2015.
- [S6] Roger Proksch, Marta Kocun, Donna Hurley, Mario Viani, Aleks Labuda, Waiman Meinhold, and Jason Bemis. Practical loss tangent imaging with amplitude-modulated atomic force microscopy. *Journal of Applied Physics*, 119(13):134901, April 2016.